Applied Physics A (2020) 126:213
https://doi.org/10.1007/s00339-020-3368-0

Applied Physics A
Materials Science & Processing

S.I. : CURRENT STATE-OF-THE-ART IN LASER ABLATION

Development of laser ablation absorption spectroscopy for nuclear fuel materials: plume expansion behavior for refractory metals observed by laser-induced fluorescence imaging spectroscopy

Masabumi Miyabe[1] · Masaki Oba[1] · Katsuaki Akaoka[1] · Masaaki Kato[1] · Shuichi Hasegawa[2] · Ikuo Wakaida[1]

Received: 16 October 2019 / Accepted: 1 February 2020 / Published online: 20 February 2020

Abstract
The dynamic behavior of an ablation plume in low pressure rare gas ambient was investigated with laser-induced fluorescence imaging spectroscopy for three refractory metals, i.e. titanium, zirconium and hafnium. A comparison of the plume expansion behaviors for the species of these elements revealed an atomic weight effect on the plume structure formation. A hemispherical thin layer and cavity structure reported previously for gadolinium were observed also for these elements. It was found that the plume size increases as well as the layer thickness decreases with increasing atomic weight. For ground state atoms of Ti, substantial amount of atoms were observed even at the center of the plume. Also, the persistence of the Ti atomic plume was as long as 300 μs, which was significantly longer than the other species studied. Furthermore, the mass-dependent elemental separation was observed in the ablation plume produced from a multielement sample. These results suggest that the observed plume structure arises from the ion-electron recombination process and the recoil of the ablated species during the multiple collisions with gas atoms.

Keywords Laser-induced fluorescence spectroscopy · Laser ablation · Ablation plume structure · LIBS · Refractory metals

1 Introduction

Laser ablation is one of the promising laser technologies having vast application field, for instance pulsed laser deposition (PLD) [1], nanoparticle synthesis [2], laser cutting [3] and so on. Even for analytical applications, various techniques have been developed since 1970s based on this process. In earlier period, it was combined with the ICP plasma torch [4, 5] as an atomization technique for analytes; lately, laser-induced breakdown spectroscopy (LIBS) in which the elemental composition can be determined from the emission intensity of the laser induced plasma has gradually gained popularity. However, as is often pointed out, a typical limit of detection (LOD) for standard LIBS is reported to be ppm order, which is insufficient for some demands. To overcome this difficulty, various advanced LIBS techniques such as double-pulse LIBS [6], combined LIBS and Laser-induced fluorescence (LIF) [7, 8], Resonance LIBS [9], spark-assisted LIBS [10] and microwave-assisted LIBS [11] have been developed, so that currently the attainable LOD reaches to ppb order. In addition, the absorption spectroscopy (LAAS) and LIF spectroscopy for ablation plume have also been applied to the isotope analysis requiring higher spectroscopic resolution [12–21].

For these developments, the knowledge on plume expansion behavior of ablated species is of great importance. We have investigated plume dynamics of ablated heavy element species to develop remote isotope analysis of nuclear fuel by means of LAAS and LIF techniques [22–26]. Since the plume expansion significantly decelerates in background gas, to know the spatiotemporal distribution of target species is indispensable for improving spectral resolution as well as detection sensitivity. From these studies, it was revealed that for the plume produced in gas ambient, the atoms and ions in ground states accumulate in a hemispherical thin layer around plume periphery, and a cavity containing a lower density of ablated species is formed near the center of the

✉ Masabumi Miyabe
miyabe.masabumi@jaea.go.jp

[1] Remote Analytical Technology Group, Collaborative Laboratory for Advanced Decommissioning Science, Japan Atomic Energy Agency, Shirakata 2-4, Tokai-mura, Naka-gun, Ibaraki-ken 319-1195, Japan

[2] Department of Nuclear Engineering and Management, The University of Tokyo, Hongo 7-3-1, Bunkyo-ku, Tokyo, Japan

plume. In addition, it was suggested that the plume structure was formed as a consequence of ion-electron recombination and recoil of ablated species through multiple collisions with gas atoms.

In our previous LAAS study we have investigated only heavy elements, since major components of nuclear fuel are actinide elements, and also lanthanides are usually used as surrogates for the actinides. However, as expected from the fact that the plume structure arises from recoil of ablated species through multiple collisions, the distribution of lighter elements in a plume is expected to be different from that of heavier elements, and the information is possibly needed for spectroscopic analyses for impurities in nuclear fuels.

In the present study, to reveal the difference in plume expansion behavior with respect to the physical properties of ablated atoms, we observe plume structure of three refractory metals i.e. Ti, Zr and Hf in He ambient by means of LIF imaging spectroscopy. These elements were chosen because their optical and thermodynamic properties are similar, which is suitable to study the atomic weight effect on plume structure formation. From the cross-sectional fluorescence images of the plume measured with sheet-shaped probe beam, we reveal the atomic weight effect on the formation of hemispherical layer and cavity, and also we discuss the underlying mechanisms which govern the plume expansion into gas ambient.

2 Experimental

Figure 1 shows an experimental setup for LIF imaging spectroscopy. The second harmonic radiation from an Nd:YAG laser (Spectra Physics, INDI-10, 532 nm, 8 ns) was delivered to a vacuum chamber, and then focused normally on a refractory metal chip (High Purity Chemicals, 10 mm × 10 mm, 1 mm thickness) with a lens of 200 mm focal length. The lens–sample distance was adjusted to place the focal point at a position approximately 1 mm behind the surface of the sample. The sample stage was rotated at a rate of about 2 rpm to avoid the crater effect. The pulse energy was monitored during measurements using a pyroelectric detector (Ophir PE-30), and was adjusted by rotating the linear polarization angle of the

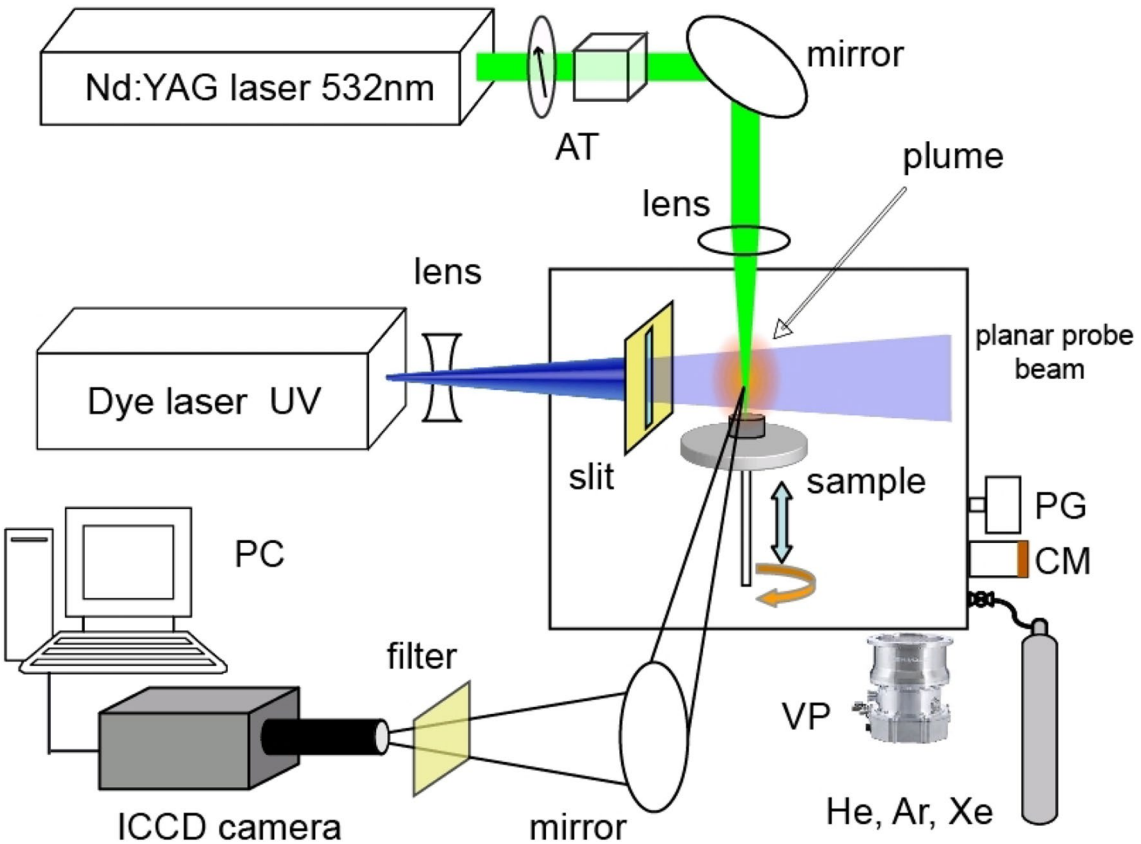

Fig. 1 Experimental setup for LIF imaging spectroscopy. VP, PG, CM and AT mean vacuum pump, convection-enhanced Pirani gauge, capacitance manometer and attenuator consisting of polarizing beam-splitter cube and half-wave plate. LIF images of ablation plume were acquired with an ICCD camera from an orthogonal direction to the planar probe beam

beam with respect to a polarizing beam splitter cube using a half-wave plate so that the energy was set to 0.5 mJ (fluence: 1.5 J/cm^2).

Helium (purity 99.99%) was employed for the background gas. After evacuating the chamber with a vacuum pump and flushing several times with the gas, the chamber was filled with the gas, and the pressure was maintained constant (800 Pa) owing to continuous pumping and gas flow. The pressure was monitored with a capacitance manometer (MKS, Baratron), and the flow rate was controlled with a flow regulating valve.

The produced ablation plume was subsequently intersected with a probe beam from a tunable dye laser (Sirah, Cobra-Stretch, bandwidth: 3 GHz, DCM dye) that was equipped with a harmonic generator (BBO) and was pumped by another Nd:YAG laser (Spectra Physics, INDI-10). The pulse energy of the UV probe beam was set at approximately 0.1 mJ with a neutral density filter.

The UV beam was first expanded with a quartz concave lens (focal length: −250 mm) and then converted into a thin sheet-shaped beam by passing through a slit (gap width: 0.5 mm) located in front of the sample to avoid generating interference fringes. When the dye laser was tuned to a resonance wavelength of each species, fluorescence was emitted from the portion of the plume irradiated by the probe beam. In the present study, we chose six intense excitation transitions originating from atoms and ions of each element in the ground states or low-lying metastable states (hereafter ground states) and lying in the 307–320 nm wavelength range, as listed in Table 1. The fluorescence transitions used to measure the images were chosen considering the magnitude of the branching ratio and the wavelength difference from the excitation transition.

LIF images were obtained using an intensified CCD (ICCD) camera (Andor, DH334T-18F-03) from a direction orthogonal to the probe beam. The spatial resolution of the image is estimated to be around 100 µm, which is limited by the focus of the camera. Placing an interference filter (Edmund) in front of the camera, LIF images with higher contrast were obtained by blocking the plasma emission from the plume and stray light from the Nd:YAG lasers. Table 2 summarizes the specification of the interference filter utilized for each species. For measurement of the UV fluorescence image, UV grade optics (lens, windows, and mirrors) were used between the camera and the plume.

Figure 2 schematically shows the firing timing of the ablation and probe lasers along with the gate timing of the camera. These timings were controlled using a multichannel delayed pulse generator (SRS, DG645). The plume observation timing was adjusted by varying the delay time between the 8 ns probe pulse and the 8 ns ablation pulse generally in the range 0.1–5.0 µs. Additionally, from a preliminary experiment, the gate delay of the camera after irradiation

Table 1 Spectroscopic data relevant to the present study

Species	(a) Dye laser excitation transition							(b) LIF observation transition					
	Wavelength air (nm)	gf	BR	$A\times10^7$ (1/s)	Lower (cm^{-1})	J_L	Upper (cm^{-1})	J_U	Wavelength air (nm)	gf	BR	$A\times10^7$ (1/s)	Lower (cm^{-1})	J_L
Ti atom	318.6451	0.85	0.57	7.98	0.0	2	31,373.8	3	503.8399	1.03	0.27	3.87	11,531.8	2
Ti ion	307.2122	0.22	0.10	1.98	225.7	3.5	32,767.1	3.5	430.0049	0.17	0.04	0.77	9518.1	2.5
Zr atom	319.1231	0.42	0.36	3.90	0.0	2	31,326.8	3	507.8313	0.76	0.26	2.80	11,640.7	2
Zr ion	311.0871	0.10	0.06	0.84	763.4	3.5	32,899.5	3.5	435.9720	0.35	0.11	1.51	9968.7	2.5
Hf atom	307.2879	0.45	0.70	4.51	0.0	2	32,533.3	3	331.2868	0.18	0.24	1.54	2356.7	3
Hf ion	314.5310	0.03	0.10	0.52	0.0	1.5	31,784.2	1.5	347.9289	0.09	0.25	1.26	3050.9	2.5
								[a]	355.2707	0.11	0.28	1.42	3644.7	1.5

6th and 14th columns denote lower level energies and 7th and 15th columns denote total angular momentum of the lower level, 8th and 9th columns denote level energy and total angular momentum of the common upper level, and second and 10th columns denote excitation and fluorescence transition wavelengths. Wavelengths, oscillator strengths (gf), transition probabilities (A) and transition assignments were taken from [30]

[a]For Hf ion, two transitions can be observed with the interference filter utilized

Table 2 Specifications of interference filters utilized

Species	Center wavelength (nm)	Pass band (nm)	Transmittance (%)
Ti atom	500	10	> 45
Ti ion	430	10	> 40
Zr atom	510	10	> 45
Zr ion	436	10	> 40
Hf atom	350	40	> 25
Hf ion	350	40	> 25

by the probe laser and the gate width were optimized to be 10 ns and 100 ns, respectively.

We used the image processing software package (Andor, SOLIS) for analysis of the acquired images. Despite the use of interference filters several plasma emission lines lie in the narrow transmission band. Hence, we imaged the plasma emission alone by blocking the probe laser beam after obtaining LIF images; by subtracting the emission image from the corresponding LIF image using the image processing software, higher contrast LIF images were obtained.

3 Results and discussion

3.1 Temporal evolution of plume structure

The cross-sectional fluorescence images of Hf, Zr, and Ti species were acquired in the delay time range of 0.1–100.0 μs under equivalent conditions for our previous study with Gd metal samples (background gas: 800 Pa He, ablation energy: 0.5 mJ) [25]. The obtained images of ions and atoms are shown in Figs. 3a–c and 4a–c, respectively. For comparison, each LIF image is normalized by its own maximum intensity, whereas, in actuality, the intensity rapidly decreases with time. The actual physical size of each image is approximately 9 mm × 9 mm. Compared to Zr and Ti, the Hf images are slightly hazy. This is because the passband of the filter for Hf is wider (see Table 2) so that the LIF image is still overlapped with the weak emission image after the subtraction of the emission image described above. Figures 5 and 6 show the fluorescence intensity distributions along the surface normal (longitudinal) direction. These profiles were obtained from Figs. 3 and 4 by averaging the data over a 150 μm width along the surface normal axis to improve the signal-to-noise ratio. In these figures, all plots were drawn according to a common intensity scale; thus, the intensity variations can be compared throughout the progression of plume evolution.

As observed previously with Gd metal sample, the ablated ground state atoms and ions of refractory metals accumulate in a hemispherical boundary layer between the plume and the ambient gas, and a cavity containing lower density of ablated species is formed in the region surrounded by the layer, particularly at later expansion stages. In contrast, during the early expansion stages only the inner components of atoms and ions are observed above the ablation spot. At 0.1 μs, the inner component of ions is unidirectional whereas that of atoms is isotropic. The difference in these shapes is attributed to the difference in their initial ejection velocities from the sample surface. In the case of ions, hemispherical shape thin layer surrounding this inner component appears at 0.3 μs, whereas in the case of atoms, the similar layer gradually appears after 0.5 μs. While the layer appearance timing is different, the locations of the layers are nearly identical. This coincidence of the appearance locations of the layers strongly suggests that neutral atoms in the layer are produced from singly charged ions through an ion-electron recombination process. In addition, the inner component gradually

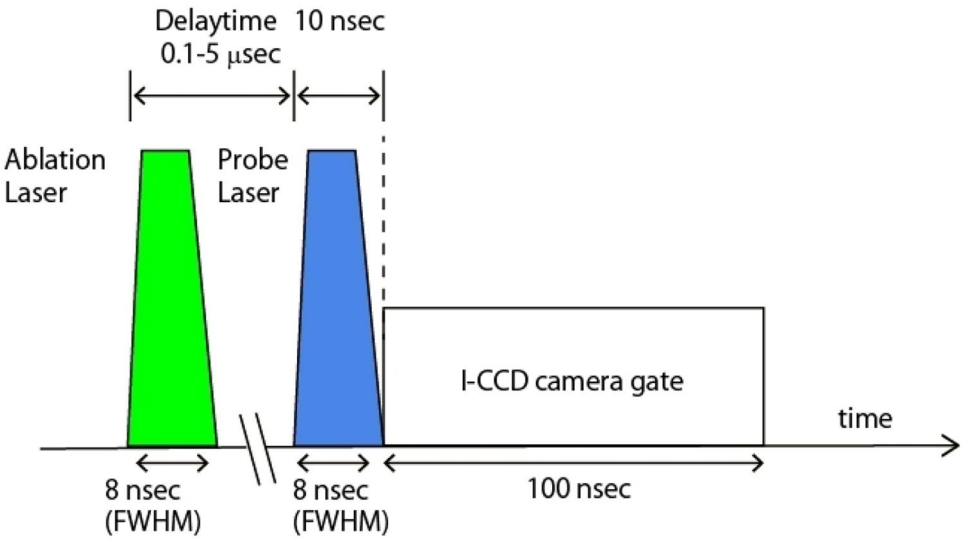

Fig. 2 Laser firing and camera gate timings

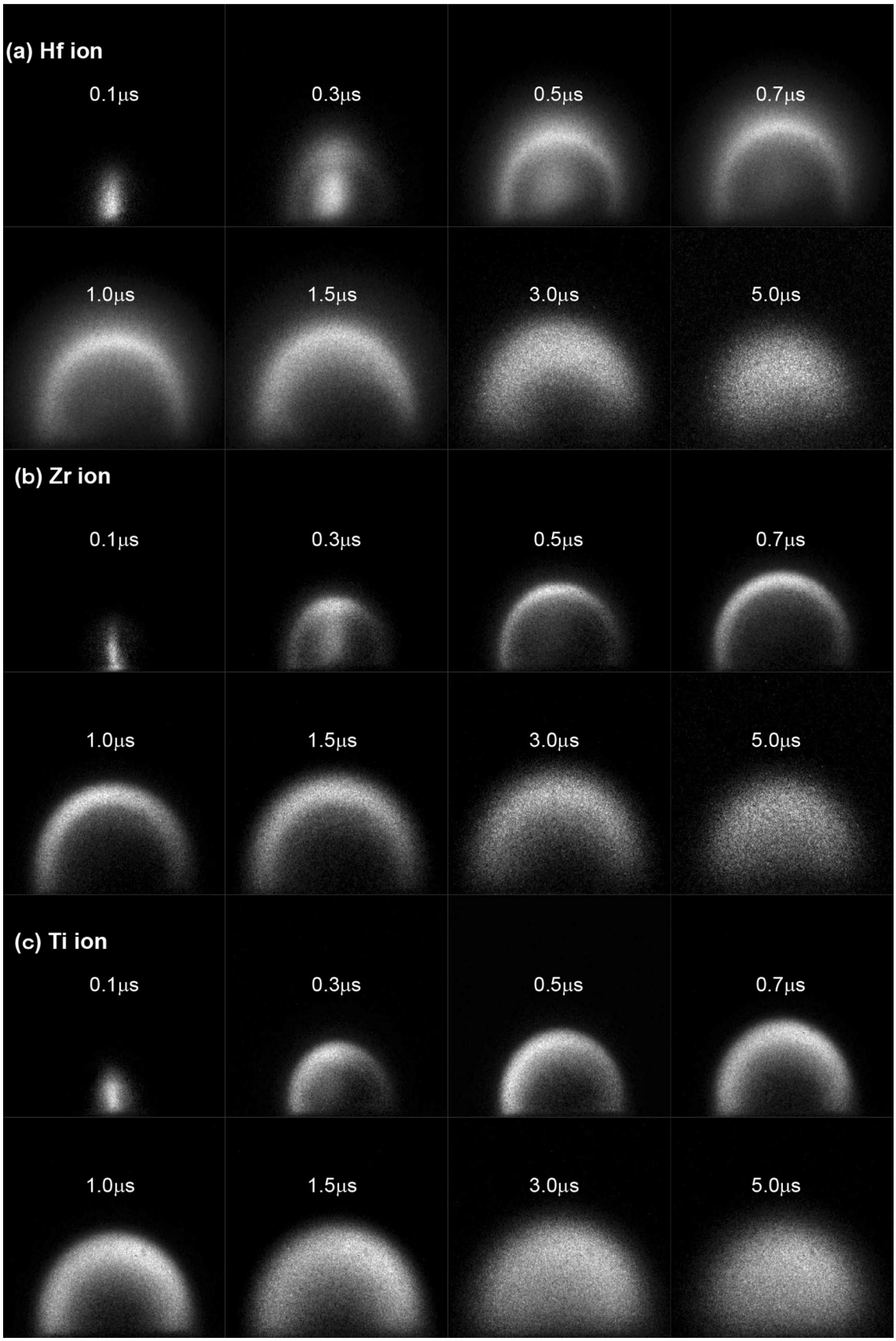

Fig. 3 Temporal evolution of the ablation plume for ground-state ions of Hf **a**, Zr **b** and Ti **c** under an 800 Pa He ambient and ablation energy of 0.5 mJ

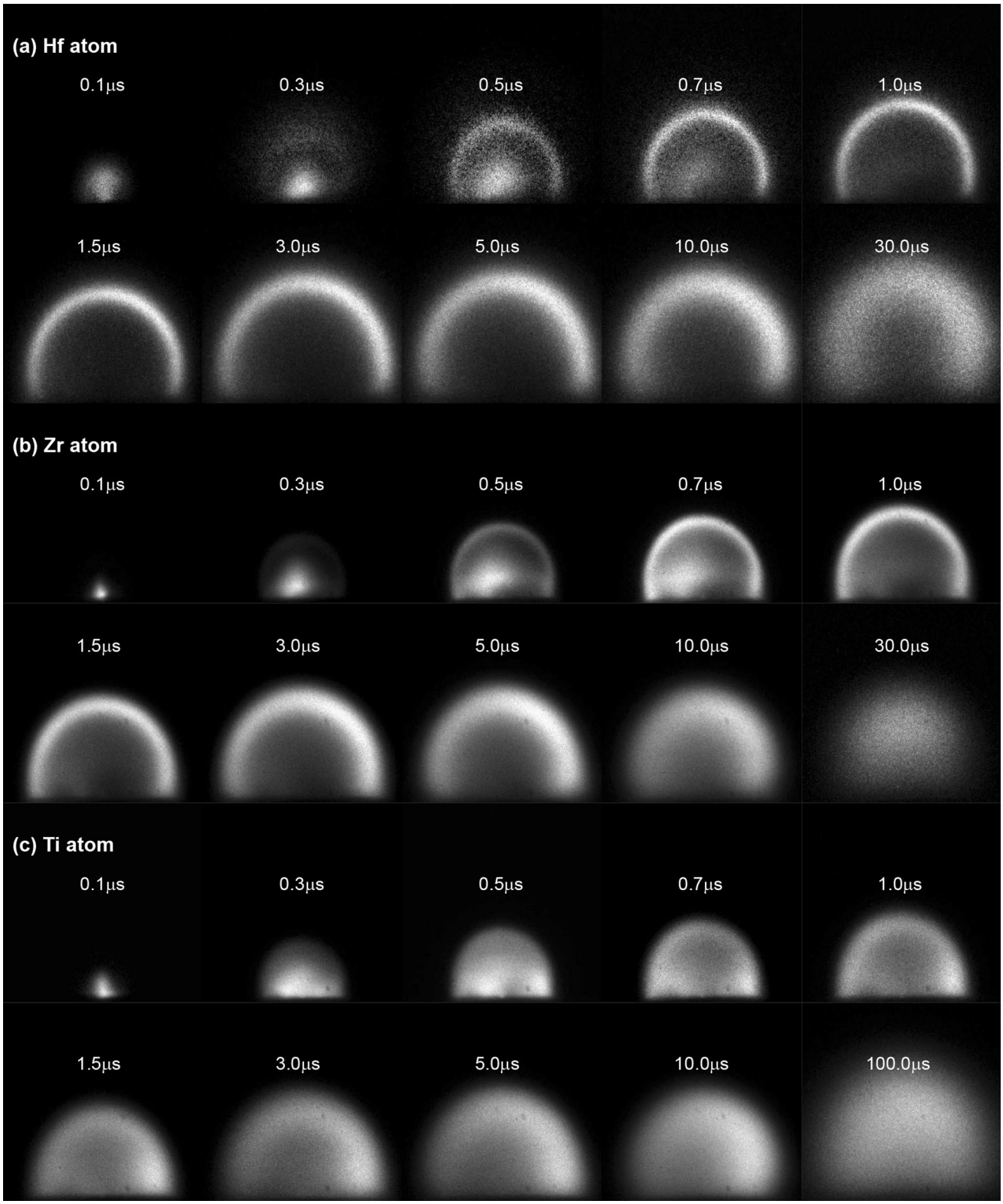

Fig. 4 Temporal evolution of the ablation plume for ground-state atoms of Hf (**a**), Zr (**b**) and Ti (**c**) under an 800 Pa He ambient and ablation energy of 0.5 mJ

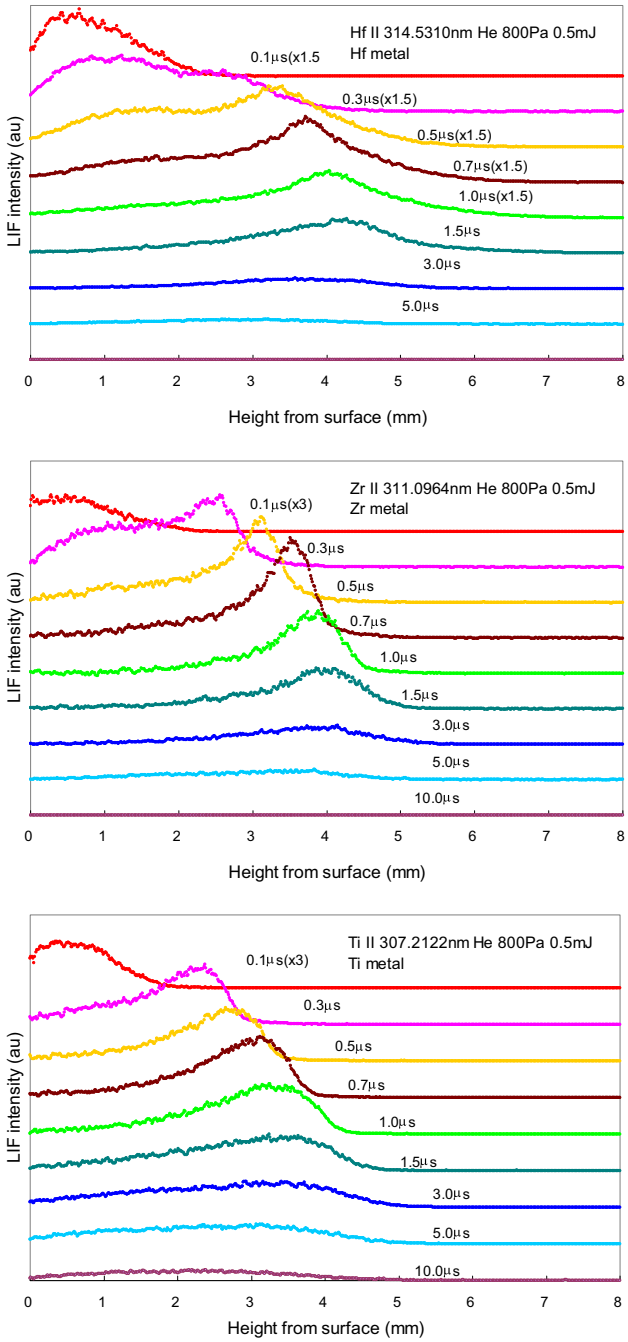

Fig. 5 Longitudinal fluorescence intensity distributions for ions of Hf (**a**), Zr (**b**) and Ti (**c**) under an 800 Pa He ambient and ablation energy of 0.5 mJ. All plots were drawn using a common intensity scale, and the intensity variation can be compared throughout the plume evolution

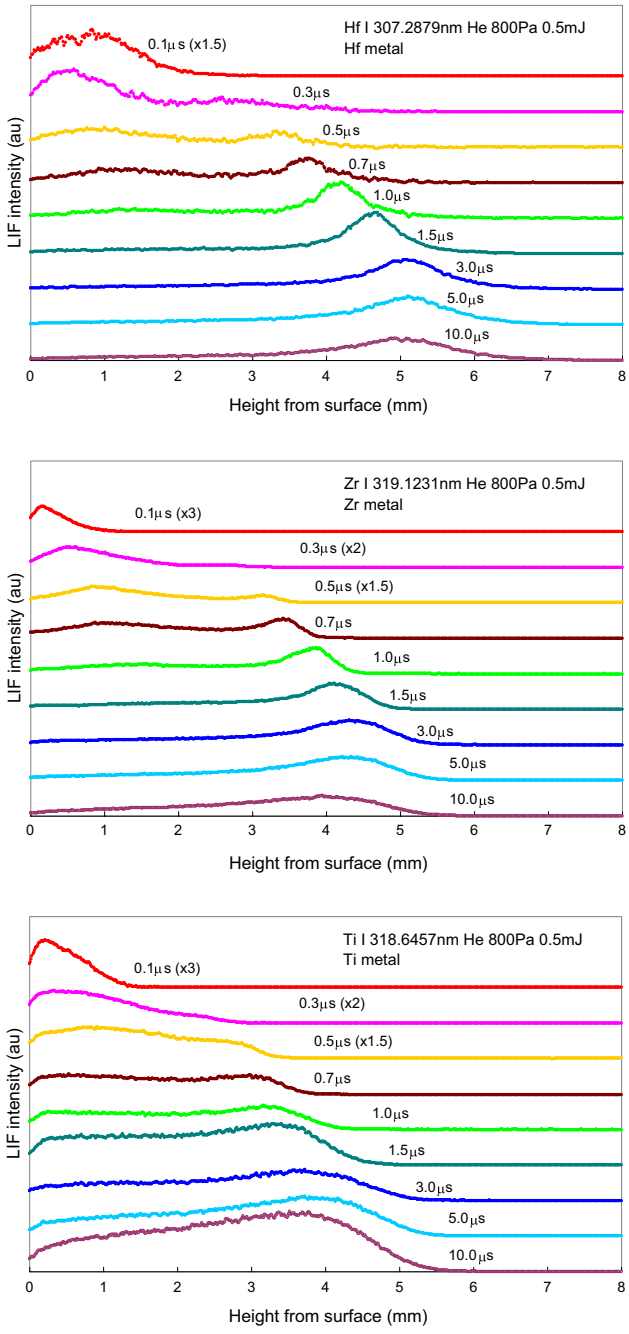

Fig. 6 Longitudinal fluorescence intensity distributions for atoms of Hf (**a**), Zr (**b**) and Ti (**c**) under an 800 Pa He ambient and ablation energy of 0.5 mJ. All plots were drawn using a common intensity scale, and the intensity variation can be compared throughout the plume evolution

diffuses in the cavity and vanishes, forming a simple plume structure after 1.0 μs.

The observed two-component plume structure has been reported by many researchers. Among them a famous early study using emission imaging technique was made by Geohegan [27]. His study revealed that a considerably slowed, highly luminous contact front component appeared in the gas-plume boundary, and that inside the plume there is also an internal component being hardly decelerated and eventually coalesced into the front component. In the hemispherical layer, most of the neutral atoms are generated through recombination, and they are initially populated in highly

excited states, and radiatively decay toward ground state through cascade pathways. Thus, it is considered that the front component appeared in his emission images corresponds to a part of the hemispherical layer observed in the present study, and the internal components observed in both emission and fluorescence images are almost the same.

At a later expansion stage shown in Fig. 3, the ionic plume boundary becomes unclear and shrinks slightly prior to its disappearance. This behavior is apparent when comparing the images of atoms and ions at 5 μs. This is most probably because the ions in the plume periphery is tend to be neutralized and disappear more readily owing to three-body recombination process occurring around the contact layer between plume and ambient gas [25].

3.2 Expansion behavior specific for refractory metals and atomic weight effect on plume structure

In comparison to the Gd metal images, the most notable difference in the refractory metal images is the longer persistence of atomic plume. It was found that the persistence for Hf and Zr atomic plume is around 50 μs and that for Ti atomic plume is as long as 300 μs although not shown in Fig. 4. This difference is likely to arise because Gd is easily oxidizable metal.

It is worth noting that there are atomic weight effects on hemispherical layer thickness and plume size. For example, from Fig. 5, the thicknesses at a delay time of 1 μs are estimated to be 400, 700 and 2000 μm (full width at half maximum) for Hf, Zr, and Ti atoms, respectively. This thickness of Hf atom is close to that of Gd atom which has been reported to be 500 μm at 1 μs delay [25].

Moreover, to compare the plume size, atomic plume images of refractory metals at 1.5 μs are shown in Fig. 7a along with that of Gd metal. From this figure, it is seen that the plume for heavier atoms is apparently larger. These atomic weight effects are attributed to the degree of recoil during multiple collisions between ablated species and gas atoms. For the atoms much heavier than He, such as Hf, even if they collide with He atoms during plume expansion, the decreases in their kinetic energies are negligible, and they still continue to displace the background gas around the contact layer. On the other hand, relatively lighter atoms such as Ti are greatly decelerated through the collisions so that the decelerated atoms come to rest behind the expanding contact front, producing a thicker hemispherical layer. Furthermore, the loss of their kinetic energy results in a smaller plume size for lighter element. In our previous studies, the atomic weight effect was investigated by changing kinds of ambient gases, i.e. He, Ar, and Xe. However, in that case, the pressure of each gas was adjusted to produce nearly equivalent final plume sizes; thus we observed only the atomic weight effect on the layer thickness. The present cross-sectional fluorescence images of three refractory elements clearly show the atomic weight effect on plume size.

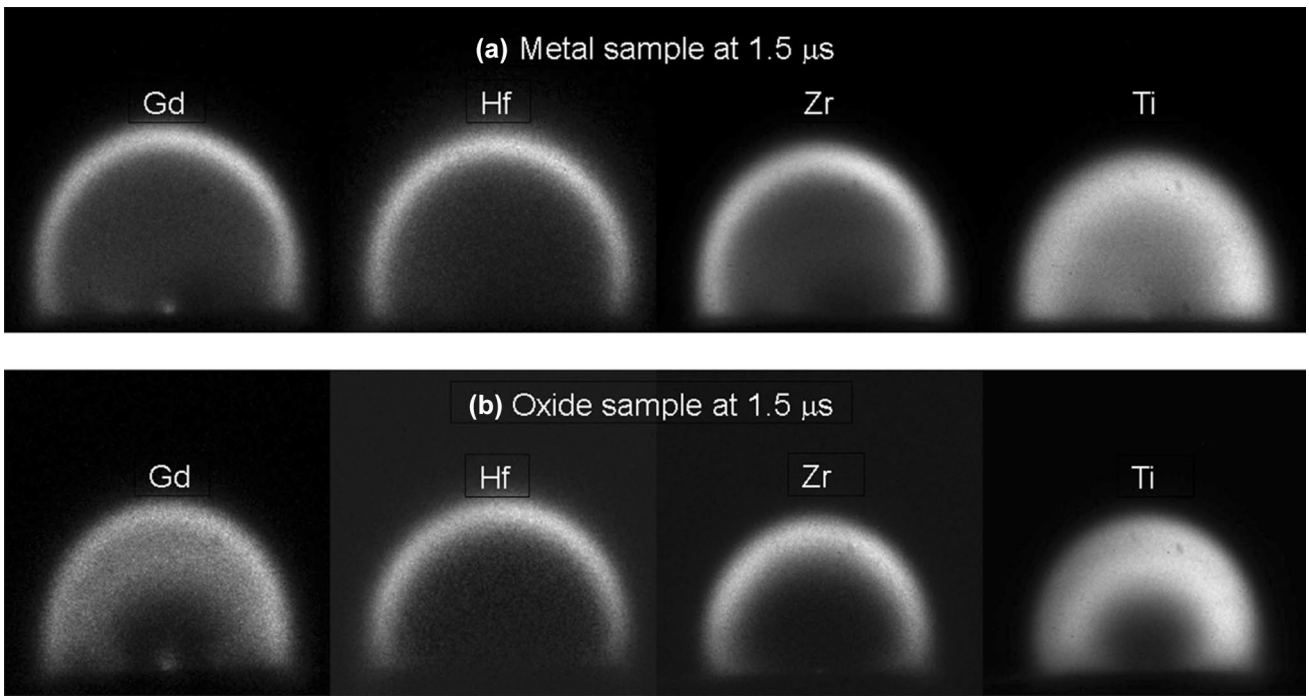

Fig. 7 LIF images for various species observed with **a** metal and **b** mixed oxide samples at 1.5 μs delay for ablation energy of 0.5 mJ

Interestingly, as shown in Fig. 4c, only the cavity for Ti atomic plume is not so clear in any plume expansion stages. This is presumably because the number density of Ti atoms in the inner component is significantly higher than the other species. Since this component diffuse isotropically, a part of them coalesce into the hemispherical layer, which make difficult to identify cavity structure. In contrast, inner component of Ti ions is sparse so that the cavity can be observed clearly. The disappearance of atoms in the plume proceeds through some reactions, i.e. clustering, oxidization, condensation, whereas that of ions occurs mainly through recombination process. These reaction rates and the resultant persistence of ablation plume depend on the collision frequency of ablated species. Thus, the observed significantly longer persistence of Ti atomic plume may be interpreted by the fact that many of the ablated atoms stay inside the cavity where very few atoms collide with gas atoms.

Considering the atomic weight effect on the plume structure and the high particle density of the inner components of Ti atoms described above, it is inferred that separation of each element occurs in the ablation plume produced from a multielement sample. To ascertain this separation, we made sintered pellets by uniformly mixing oxide powders of three refractory metals so as to observe the LIF images of the plume produced under the same conditions as Fig. 7a. The result is shown in Fig. 7b. The reasons of the reduction in plume size for this oxide sample are most probably that oxygen atoms generated from the pellet readily deplete ablated atoms in the plume [28, 29], and that some chemical reactions in the plume partly consume the ablation energy. As shown in this figure, also for the mixed oxide pellet, the atomic weight effect on particle distribution was observed. This result suggests that an elemental fractionation may occur when only a part of the plume, especially plume periphery, is observed with LIBS or LAAS. The information on the distribution of different kinds of species in the plume will be useful also for various applications using ablation process such as thin film deposition, nanoparticle synthesis and so on.

4 Conclusion

To reveal the difference in plume expansion characteristics with respect to the physical properties of ablated atoms, we observed plume structure of high refractory metals i.e. Ti, Zr and Hf in He ambient by means of LIF imaging spectroscopy. From the observed cross-sectional LIF images of the ablation plume, it was found that the plume size increases and the layer thickness decreases with increasing atomic weight. In addition, for Ti atoms, the number density in the inner component was significantly higher than the other species. Furthermore, we observed that mass-dependent elemental separation occurs in the ablation plume produced from multielement sample. From these results, it is inferred that an elemental fractionation may occur when only a part of the plume is observed with LIBS or LAAS.

Acknowledgements The present study is financially supported by JSPS KAKENHI Grant Number JP18H01922 and the Nuclear Energy Science & Technology and Human Resource Development Project (through concentrating wisdom) from the Japan Atomic Energy Agency/Collaborative Laboratories for Advanced Decommissioning Science.

References

1. D.B. Chrisey, G.K. Hubler (eds.), *Pulsed Laser Deposition of Thin Films* (Wiley, New York, 1994)
2. I. Umezu, N. Sakamoto, H. Fukuoka, Y. Yokoyama, K. Nobuzawa, A. Sugimura, Effects of collision between two plumes on plume expansion dynamics during pulsed laser ablation in background gas. Appl. Phys. A **110**, 629 (2013)
3. F. Ullmann, U. Loeschner, L. Hartwig, D. Szczepanski, J. Schille, S. Gronau, T. Knebel, J. Drechsel, R. Ebert, H. Exner, High-speed laser ablation cutting of metal. Proc. SPIE **8603**, 860311 (2013)
4. S.F. Durrant, Laser ablation inductively coupled plasma mass spectrometry: achievements, problems, prospects. J. Anal. At. Spectrom. **14**, 1385–1403 (1999)
5. R.E. Russo, X. Mao, H. Liu, J. Gonzalez, S.S. Mao, Laser ablation in analytical chemistry—a review. Talanta **57**, 425–451 (2002)
6. V.I. Babushok, F.C. DeLucia Jr., J.L. Gottfried, C.A. Munson, A.W. Miziolek, Double pulse laser ablation and plasma: laser induced breakdown spectroscopy signal enhancement. Spectrochim. Acta B **61**, 999 (2006)
7. F.H. Kortenbruck, R. Noll, P. Wintjens, H. Falk, C. Becker, Analysis of heavy metals in soils using laser-induced breakdown spectrometry combined with laser-induced fluorescence. Spectrochim. Acta B **56**, 933 (2001)
8. H.H. Telle, D.C.S. Beddows, G.W. Morris, O. Samek, Sensitive and selective spectrochemical analysis of metallic samples: the combination of laser-induced breakdown spectroscopy and laser-induced fluorescence spectroscopy. Spectrochim. Acta B **56**, 947 (2001)
9. K. Rifai, F. Vidal, M. Chaker, M. Sabsabi, Resonant laser-induced breakdown spectroscopy (RLIBS) analysis of traces through selective excitation of aluminum in aluminum alloys. J. Anal. At. Spectrom. **28**, 388 (2013)
10. O.A. Nassef, H.E. Elsayed-Ali, Spark discharge assisted laser induced breakdown spectroscopy. Spectrochim. Acta B **60**, 1564–1572 (2005)
11. K. Ali, M. Tampo, K. Akaoka, M. Miyabe, I. Wakaida, Enhancement of LIBS emission using antenna-coupled microwave. Opt. Express **21**, 29755–29768 (2013)
12. I.B. Gornushkin, L.A. King, B.W. Smith, N. Omenetto, J.D. Winefordner, Line broadening mechanisms in the low pressure laser-induced plasma. Spectrochim. Acta B **54**, 1207–1217 (1992)
13. H. Liu, A. Quentmeier, K. Niemax, Diode laser absorption measurement of uranium isotope ratios in solid samples using laser ablation. Spectrochim. Acta B **57**, 1611–1623 (2002)
14. B.A. Bushaw, N.C. Anheier Jr., Isotope ratio analysis on micron-sized particles in complex matrices by laser ablation-absorption ratio spectrometry. Spectrochim. Acta B **64**, 1259–1265 (2009)
15. N.R. Taylor, M.C. Phillips, Differential laser absorption spectroscopy of uranium in an atmospheric pressure laser-induced plasma. Opt. Lett. **39**, 594–597 (2014)

16. S.S. Harilal, N.L. LaHaye, M.C. Phillips, Two-dimensional fluorescence spectroscopy of laser-produced plasmas. Opt. Lett. **41**, 3547–3550 (2016)
17. M.C. Phillips, B.E. Brumfield, N.L. LaHaye, S.S. Harilal, K.C. Hartig, I. Jovanovic, Two-dimensional fluorescence spectroscopy of uranium isotopes in femtosecond laser ablation plumes. Sci. Rep. **7**, 3784 (2017)
18. S.S. Harilal, N.L. LaHaye, M.C. Phillips, High-resolution spectroscopy of laser ablation plumes using laser-induced fluorescence. Opt. Express **25**, 2312–2326 (2017)
19. S.S. Harilal, B.E. Brumfield, M.C. Phillip, Standoff analysis of laser-produced plasmas using laser-induced fluorescence. Opt. Lett. **43**, 1055–1058 (2018)
20. J. Bergevin, T.-H. Wu, J. Yeak, B.E. Brumfield, S.S. Harilal, M.C. Phillips, R.J. Jones, Dual-comb spectroscopy of laser-induced plasmas. Nat Commun **9**, 1273 (2018)
21. S.S. Harilal, B.E. Brumfield, N.L. LaHaye, K.C. Hartig, M.C. Phillips, Optical spectroscopy of laser-produced plasmas for standoff isotopic analysis. Appl. Phys. Rev. **5**, 021301 (2018)
22. M. Miyabe, M. Oba, H. Iimura, K. Akaoka, Y. Maruyama, I. Wakaida, Spectroscopy of laser-produced cerium plasma for remote isotope analysis of nuclear fuel. Appl. Phys. A **101**, 65–70 (2010)
23. M. Miyabe, M. Oba, H. Iimura, K. Akaoka, Y. Maruyama, H. Ohba, M. Tampo, I. Wakaida, Doppler-shifted optical absorption characterization of plume-lateral expansion in laser ablation of a cerium target. J. Appl. Phys. **112**, 123303 (2012)
24. M. Miyabe, M. Oba, H. Iimura, K. Akaoka, Y. Maruyama, H. Ohba, M. Tampo, I. Wakaida, Absorption spectroscopy of uranium plasma for remote isotope analysis of next-generation nuclear fuel. Appl. Phys. A **112**, 87–92 (2013)
25. M. Miyabe, M. Oba, H. Iimura, K. Akaoka, A. Khumaeni, M. Kato, I. Wakaida, Ablation plume structure and dynamics in ambient gas observed by laser-induced fluorescence imaging spectroscopy. Spectrochim. Acta B **110**, 101 (2015)
26. M. Miyabe, M. Oba, K. Jung, H. Iimura, K. Akaoka, M. Kato, H. Otobe, A. Khumaeni, I. Wakaida, Laser ablation absorption spectroscopy for isotopic analysis of plutonium: spectroscopic properties and analytical performance. Spectrochim. Acta B **114**, 42–51 (2017)
27. D.B. Geohegan, Fast intensified-CCD photography of $YBa_2Cu_3O_{7-x}$ laser ablation in vacuum and ambient oxygen. Appl. Phys. Lett. **60**, 2732–2734 (1992)
28. P.J. Skrodzki, N.P. Shah, N. Taylor, K.C. Hartig, N.L. LaHaye, B.E. Brumfield, M.C. Phillips, S.S. Harilal, Significance of ambient conditions in uranium absorption and emission features of laser ablation plasmas. Spectrochim. Acta B **125**, 112–119 (2016)
29. T. Okada, N. Shibamaru, Y. Nakayama, M. Maeda, Investigations of behavior of particles generated from laser-ablated $YBa_2Cu_3O_{7-x}$ target using laser-induced fluorescence. Appl. Phys. Lett. **60**, 941–943 (1992)
30. http://www.cfa.harvard.edu/amp/ampdata/kurucz23/sekur.html